

Subwavelength coherent imaging of periodic samples using a 13.5 nm tabletop high-harmonic light source

Dennis F. Gardner^{1*}, Michael Tanksalvala¹, Elisabeth R. Shanblatt¹, Xiaoshi Zhang², Benjamin R. Galloway¹, Christina L. Porter¹, Robert Karl Jr¹, Charles Bevis¹, Daniel E. Adams¹, Henry C. Kapteyn^{1,2}, Margaret M. Murnane^{1,2} and Giulia F. Mancini¹

Coherent diffractive imaging is unique, being the only route for achieving high spatial resolution in the extreme ultraviolet and X-ray regions, limited only by the wavelength of the light. Recently, advances in coherent short-wavelength light sources, coupled with progress in algorithm development, have significantly enhanced the power of X-ray imaging. However, so far, high-fidelity diffraction imaging of periodic objects has been a challenge because the scattered light is concentrated in isolated peaks. Here, we use tabletop 13.5 nm high-harmonic beams to make two significant advances. First, we demonstrate high-quality imaging of an extended, nearly periodic sample for the first time. Second, we achieve subwavelength spatial resolution (12.6 nm) imaging at short wavelengths, also for the first time. The key to both advances is a novel technique called ‘modulus enforced probe’, which enables robust and quantitative reconstructions of periodic objects. This work is important for imaging next-generation nano-engineered devices.

Short-wavelength light in the extreme-ultraviolet (EUV) and soft X-ray regions of the spectrum is attractive for high-resolution imaging, due to the inherent elemental and chemical-specific contrast in this spectral region resulting from electronic resonances^{1–3}. Recent advances in coherent short-wavelength light sources, including tabletop high-harmonic generation^{4–6} and large-scale synchrotron and free-electron laser facilities⁷, combined with coherent imaging methods, is leading to unique new imaging capabilities^{8–15}. Coherent diffractive imaging (CDI) techniques^{16,17} are particularly attractive for EUV and X-ray imaging, because they address critical limitations in short-wavelength imaging: indeed, most X-ray optics are costly, imperfect, lossy and cannot reach diffraction-limited spatial resolution¹⁸. Fortunately, by using CDI, it is now possible to achieve diffraction-limited spatial resolution at short wavelengths for the first time. Moreover, CDI is the most photon-efficient form of imaging because there are no optics between the sample and the detector¹⁹.

In CDI, the amplitude of the scattered light from an object is directly collected on the detector, without the need for any image-forming optics. Although the phase of the light is lost by recording only the diffracted intensity, this can be recovered computationally using iterative phase-retrieval algorithms^{20–26}. Once the phase of the light is known, the diffracted light can be computationally propagated to the sample plane to retrieve a complex-valued image of the object. For the algorithm to converge to a unique solution, the diffraction intensity must be adequately sampled at the spatial Nyquist frequency to regain phase information in the complex-valued diffraction signal²⁷. Initial implementations of CDI used mostly pinhole-like test samples that permitted the use of an isolation constraint on the object itself, facilitating phase retrieval^{17,28}. However, because the object was isolated, these approaches to CDI could not easily be used to image extended objects of relevance to material science and other applications. Furthermore, these approaches cannot separate the illumination from the object.

More recently, a particularly powerful approach to CDI known as ptychography^{29–33} has made it possible to image extended objects by acquiring multiple diffraction patterns from overlapping areas of the sample. Redundant information collected during the scan is harnessed to reconstruct the amplitude and the phase of the sample, as well as the amplitude and phase of the illuminating wave (that is, the probe)^{31,34}. Using ptychography, the isolation constraint is applied directly to the illumination beam instead of the sample, thus enabling diffraction-limited full-field imaging of complex extended objects^{35,36}. For non-periodic samples, ptychography can reliably solve for the sample and illumination simultaneously. However, periodic samples pose a particular challenge due to the lack of diversity in the diffraction patterns, resulting in poor convergence of the phase-retrieval algorithm^{16,17,27,31,37,38}. Moreover, the spatial resolution achieved so far has been limited to 1.3 times the wavelength for real-world objects under good reconstruction conditions³⁶.

In this Article, for the first time we achieve a subwavelength resolution of 0.9λ of an extended sample in the EUV region using a tabletop 13.5 nm high-harmonic light source. We also demonstrate high-fidelity, full-field, quantitative imaging of near-periodic objects for the first time. The key to achieving high-fidelity imaging of periodic samples is a novel technique we termed a ‘modulus enforced probe’ (MEP). MEP is based on collecting a single image of the unscattered direct beam on the detector. This additional measurement is then used within a novel algorithm based on the extended ptychographic iterative engine (ePIE)³⁴ to highly constrain the guess for the illumination beam. Crucially, because the total power in the input beam is measured by recording the direct beam, this method allows quantitative³⁹ amplitude and phase information retrieval for both the sample and illumination. The MEP technique also minimizes reconstruction artefacts due to crosstalk between the sample and the illumination and allows for a much faster convergence and improved robustness of the algorithm,

¹JILA, University of Colorado, 440 UCB, Boulder, Colorado 80309-0440, USA. ²Kapteyn-Murnane Laboratories, 1855 S. 57th Court, Boulder, Colorado 80301, USA. *e-mail: dennis.gardner@colorado.edu

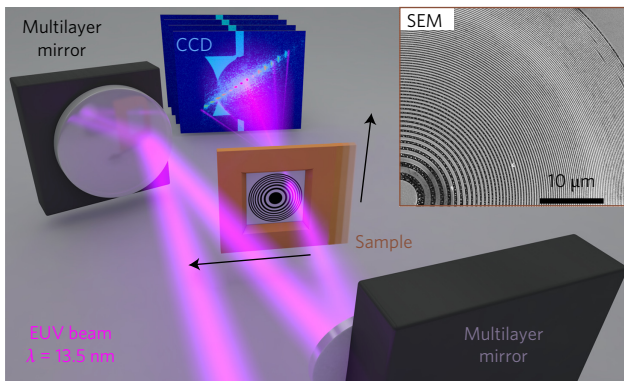


Figure 1 | MEP X-ray microscopy with 13.5 nm EUV light from a tabletop high-harmonic source. Multilayer mirrors are used to select and focus a single harmonic onto the ZP sample. Light scattered from the sample, as well as some background light, is collected on an EUV sensitive CCD. The sample is raster-scanned and the diffraction from each position is collected. Inset: SEM image of the sample.

even in the presence of noise. This experimental demonstration is, to our knowledge, the best wavelength-to-resolution ratio for any full-field, non-isolated-sample, CDI-based microscope. Finally, the 13.5 nm wavelength and the ability to reliably image near-periodic objects are technologically relevant in support of the development of next-generation EUV lithography, nanoelectronics, data storage and self-assembled nanostructures as well as functional imaging of nano-enhanced devices.

Experimental set-up and MEP methodology

We generated bright, phase-matched, high-harmonic beams (HHG)^{4–6,40} by focusing an ultrafast 800 nm laser into a helium-filled waveguide at 1 atm pressure (KMLabs XUUS 4.0). Most of the residual laser light is removed by a rejecter optic placed at an angle near glancing incidence, followed by one 600-nm-thick Zr filter. A single harmonic order at a wavelength of 13.5 ± 0.2 nm is then selected and focused onto the sample using a pair of Si/Mo multilayer mirrors (Fig. 1). The sample, a zone plate (ZP) with 150-nm-thick polymethylmethacrylate (PMMA) rings on a 50 nm silicon nitride window, was aligned perpendicular to the beam and placed at the focus (≈ 2 μm diameter, see Fig. 5). A scanning electron microscope (SEM) image of the ZP sample is shown in the inset of Fig. 1.

The sample was scanned in the focus of the EUV beam in a rectangular pattern with 121 (11 × 11) positions with nominally 0.88 μm between adjacent positions. To prevent periodic artefacts being introduced by the scan grid itself, a random offset of ±20% of the step size was added to each scan position⁴¹. At each scan position, light scattered by and transmitted through the sample is detected on a back-illuminated charge-coupled device (CCD) placed 22.6 ± 0.2 mm from the sample. As shown in Fig. 1, stray HHG light that bypasses the multilayer mirrors is also detected as background light on the detector. To maximize the numerical aperture (NA) of the microscope, the sample was scanned in the top right region, such that the strongest diffracted light scattered along the diagonal of the detector. The diffracted light was detected at an NA of 0.54. At this NA, the Abbe diffraction-limited resolution, Δr , is given by

$$\Delta r = \frac{\lambda}{2NA} = 12.5 \text{ nm} \pm 0.2 \text{ nm} \quad (1)$$

Using our novel MEP methodology, the sample was then moved out of the EUV beam path and a single image of the direct, unscattered HHG illumination was collected at the detector (Supplementary Fig. 1). This procedure can be carried out before or after acquisition of the ptychographic data set. In an alternative approach, MEP can also be applied

by separating the direct current (DC) or undiffracted beam from the rest of the diffraction pattern. This is especially effective when it is not practical to collect the direct beam on the detector—for example, due to a limited range of scanning stages, or samples that are too large to be removed from the beam path. We used the latter approach in our experiment.

The undiffracted beam was calculated by applying a 30% threshold to the scatter pattern, isolating the DC peak, which served as the MEP constraint (see Supplementary Section 5). To quantify the flux in the input beam, we statistically averaged several CCD measurements of the undiffracted beam. In a reflection geometry (rather than the transmission geometry presented in this Article), a measurement of the reflected beam off a smooth surface can be used as the undiffracted beam. If the reflectance of the reference surface is known, then the undiffracted beam data can be scaled appropriately to yield the quantitative reflectivity of the sample³⁹.

MEP algorithm implementation

Figure 2 displays the general working principle of the MEP algorithm. The MEP ptychographic experiment is composed of two data-taking steps. In the first stage, the ptychographic data set is collected by stepwise scanning of the sample in a coherent EUV beam. In the second step, the direct beam is collected at the detector by moving the sample out of the way of the incident beam. The novel probe constraint, which uses the measured probe intensity on the detector, $P_i(u)$, where u is the spatial frequency coordinate vector on the detector plane, can be implemented in many phase-diverse CDI techniques^{31,32,34,42}.

A flowchart of how the MEP constraint is employed within the ptychography algorithm at each iteration j , after updating the object and probe, is given in Fig. 2. The updated probe amplitude is propagated to the detector plane, forming a guess of the probe on the detector given by $\mathcal{P}_{Gj}(u) = \mathcal{F}[P_{j+1}(r)]$, where $P_{j+1}(r)$ is the updated probe, r is the spatial coordinate vector at the sample plane, \mathcal{F} is a propagator from the sample plane to the detector plane and $\mathcal{P}_{Gj}(u)$ is a guess of the probe at the detector plane. Here, we apply a modulus constraint to the probe guess enforcing the probe measurement. This gives

$$\mathcal{P}_{Mj}(u) = \sqrt{P_i(u)} \frac{\mathcal{P}_{Gj}(u)}{|\mathcal{P}_{Gj}(u)|^2} \quad (2)$$

This modulus-constrained probe guess is propagated back to the sample plane, \mathcal{F}^{-1} , forming a further updated probe guess:

$$P'_{Gj+1}(r) = \mathcal{F}^{-1}[\mathcal{P}_{Mj}(u)] \quad (3)$$

which is consistent with the measured probe intensity. The new probe guess, P'_{Gj+1} is now fed back into the algorithm.

This additional constraint to the probe is analogous to the error-reduction algorithm as described by Fienup²⁰, but instead of using error reduction to solve for the object, it is used within the ptychography algorithm to further constrain the probe guess. The MEP constraint provides additional information for the ptychography algorithm, thereby improving the convergence speed (see Supplementary Section 1).

Subwavelength CDI of extended near-periodic objects

Reconstructed intensity images of the ZP sample, obtained with the ePIE ptychography algorithm³⁴ with and without the novel MEP constraint, are displayed in Fig. 3b,c, respectively. The high-fidelity ptychographic reconstruction obtained with MEP (Fig. 3b) is compared to the SEM shown in Fig. 3a. The SEM image shows an inverted contrast with respect to Fig. 3b, due to the reflection mode of the SEM, as opposed to our ptychographic CDI transmission

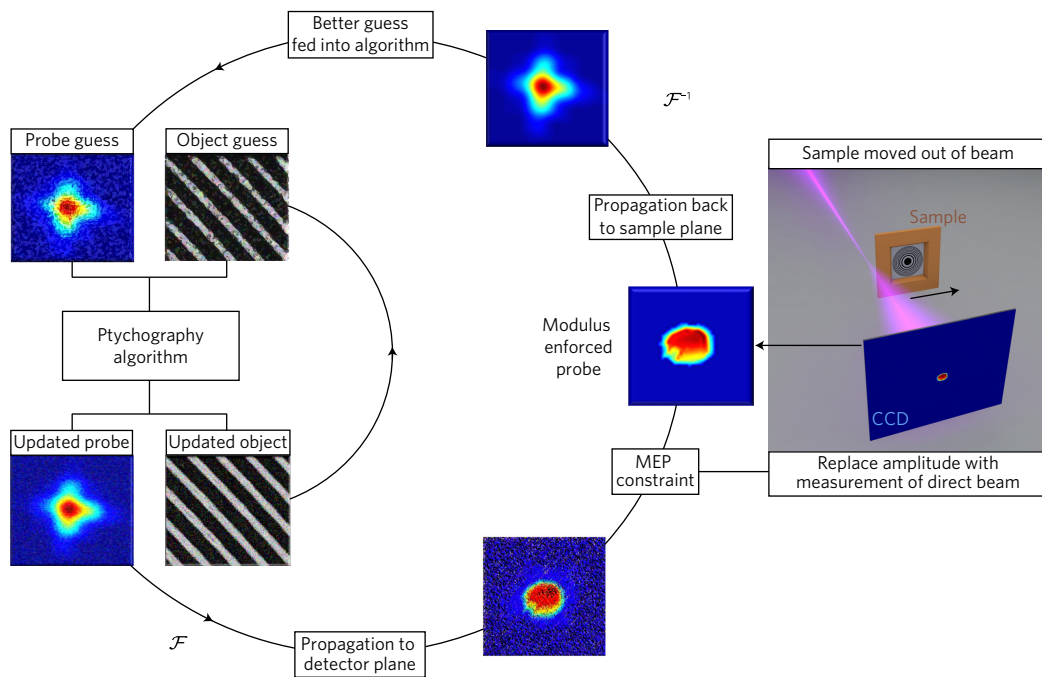


Figure 2 | Schematic layout of the MEP constraint within the ptychography algorithm. The ptychography algorithm starts with a guess of the object and probe, and then uses the set of diffraction measurements and the overlap of adjacent positions to iteratively update the object and probe guesses. The updated probe is further constrained with the measurement of the probe on the detector. This MEP-constrained probe is fed back into the ptychography algorithm, yielding faster convergence towards a unique solution.

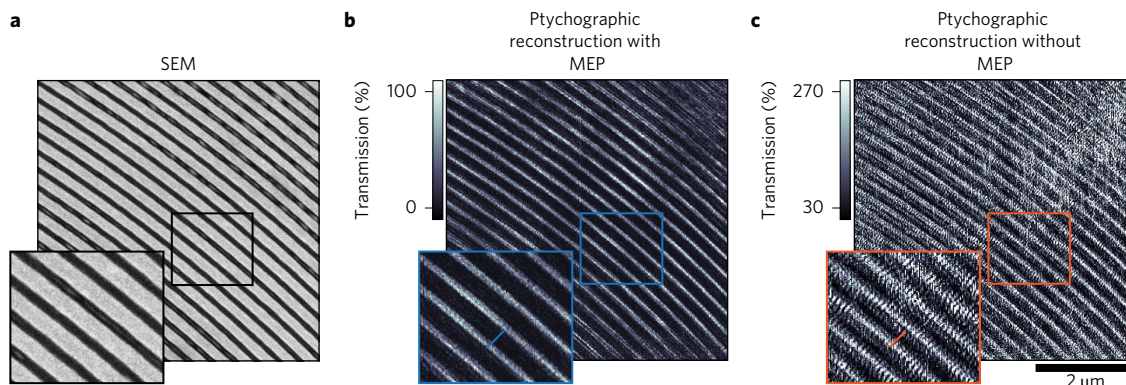


Figure 3 | Record 0.9λ subwavelength-resolution full-field imaging using 13.5 nm light and MEP. **a**, SEM image of the ZP sample. **b**, Ptychographic reconstruction of the sample, in the same region, obtained with the novel MEP constraint. The MEP constraint allows the algorithm to solve for the absolute transmissivity of the sample, which enables unique quantitative imaging capabilities. The contrast of the transmission EUV image is inverted with respect to the SEM image in **a**, obtained in reflection mode. **c**, Ptychographic reconstruction without the MEP constraint. Without the additional constraint, unphysical transmission values are obtained. The scale bar in **c** also applies to **a** and **b**.

microscope. The full, reconstructed images, as well as the retrieved phase images, are provided in the Supplementary Information.

Although the width of the rings in the ZP have a radial dependence proportional to $1/r$, with $r = 40 \mu\text{m}$ for the radius of the outermost ring, the PMMA rings within the $5.65 \times 5.65 \mu\text{m}^2$ area shown in Fig. 3b,c constitute a periodic arrangement of lines. The periodicity of these features represents a major challenge in traditional ptychographic CDI due to the lack of diversity in the diffraction patterns, leading to poor convergence of the phase-retrieval algorithms. As a result, when the MEP methodology is not applied, ringing artefacts indicated by stripes in the image are seen in the reconstruction (Fig. 3c).

The highlighted regions of Fig. 3b,c show the periodic arrangement of eight PMMA lines with $110 \pm 10 \text{ nm}$ width spaced by $90 \pm 10 \text{ nm}$ of Si_3N_4 . The high-fidelity image obtained with MEP

(blue outlined inset to Fig. 3b) is compared to the same region imaged without applying MEP (orange outlined inset to Fig. 3c) and to the image obtained with the SEM (black outlined inset to Fig. 3a). A profile across a ZP PMMA feature was selected (blue line, inset to Fig. 3b) for the reconstruction obtained with the MEP constraint. The corresponding lineout is shown in Fig. 4a as blue circles and was fitted to an error function. The 10–90% width of the fit (r^2 better than 0.97) is better than our reconstruction pixel size, dx , given by

$$dx = \frac{\lambda z}{Npx} = 12.6 \text{ nm} \pm 0.2 \text{ nm} \quad (4)$$

where λ is the wavelength, z is the distance from the CCD to the sample, N is the number of pixels on the detector and px is the

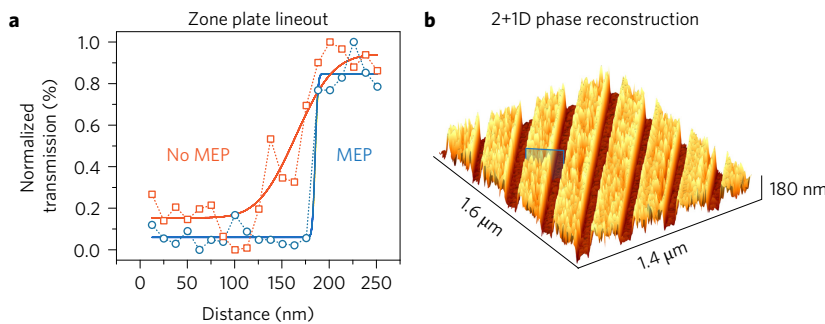


Figure 4 | Zone plate lineout and height map. **a**, Profile of a ZP feature with (blue) and without (orange) the MEP constraint. The data points of the profile are fitted to an error function. The 10–90% width from the fit of the data with the MEP constraint supports 12.6 nm subwavelength resolution. **b**, Height map of the ZP sample, obtained from the phase using the MEP constraint. The vertical scale bar has been scaled by 1/5. The blue plane shows the location of the lineout in **a**.

effective pixel size with on-chip binning. The agreement between the 12.6 nm resolution supported by the lineout of the zone plate feature and the 12.5 nm Abbe limit demonstrates that the algorithm was able to converge to a solution limited only by the NA of the data, thus demonstrating subwavelength EUV imaging for the first time.

For analysis of the reconstruction without the MEP constraint, ten parallel and adjacent profiles were averaged (orange line, inset to Fig. 3c), due to the presence of artefacts in the image. The corresponding lineout is shown by the orange squares in Fig. 4a and is fitted to an error function (r^2 better than 0.98). The 10–90% values of the fit support a 60 nm resolution without the MEP constraint.

In addition to the high spatial resolution of 0.9λ , we can also obtain topographical information from the phase images. The phase information from the inset of Fig. 3b was used to generate a three-dimensional rendering of the ZP in Fig. 4b. The reported values of PMMA⁴³ were used to calculate the height of the ZP features as 180 ± 40 nm. The phase images of the ZP are presented in the Supplementary Information (Supplementary Figs 4 and 5b).

An important implication of the enforcement of the total power of the illumination during image reconstruction is that the reconstructed amplitude image encodes the absolute transmission from the sample, as shown in Fig. 3b. This capability enables quantitative

imaging, the importance of which has been recently demonstrated with EUV reconstructed absolute phase-diverse transmissivity/reflectivity-CDI on buried layered structures³⁹.

Most importantly, the MEP constraint brings the unique capabilities of enabling reconstructions of periodic objects by minimizing the crosstalk between object and probe, as demonstrated by the smooth and continuous amplitude and phase retrieved for the illumination (Fig. 5a,b). Without the MEP constraint (Fig. 5c,d), the illumination exhibits ringing artefacts. Crosstalk between the illumination and object (Fig. 3c) is present, because the algorithm transfers power between the object and probe, which results in unreliable transmission values for the sample. Furthermore, the ptychography algorithm converges faster with the MEP constraint, especially in the presence of a poor initial probe guess, and the MEP constraint improves robustness in the presence of background. A detailed discussion on the MEP constraint effects on algorithm convergence and the effects of Gaussian and Poisson noise are reported in the Supplementary Section 1.

We note that previous work suggested subwavelength resolution in the EUV from a toy, pinhole-like sample, with algorithms that use a low degree of data redundancy and are not capable of imaging extended or periodic objects²⁸. Even for relatively thin samples, these methods do not produce reliable resolution limits, especially due to the fact that modulations in the exit surface wave can lead to artificially high spatial frequency content not found in the object. Furthermore, the estimated spatial resolution was based solely on the phase-retrieval transfer function and did not include more direct measurements like the knife-edge test.

Conclusions

We demonstrated 0.9λ spatial resolution imaging of a periodic extended object with 13.5 nm EUV light from a high-harmonic source, by applying a novel modulus enforced probe technique. Without the MEP constraint, the reconstructed image is characterized by lower fidelity (60 nm resolution) and by crosstalk between the object and the probe. With MEP, we achieve 12.6 ± 0.2 nm spatial resolution imaging, which agrees with the theoretical resolution of 12.5 ± 0.2 nm corresponding to the NA. This represents, to our knowledge, a record wavelength-to-resolution ratio for full-field imaging of an extended object with any EUV/X-ray source. Moreover, our work presents the first high-fidelity image of a periodic sample using a lensless imaging technique.

Ongoing research that requires more advanced imaging techniques such as multiplexed wavelength imaging^{11,44,45}, undersampling^{46,47} and thick samples^{48,49} will all benefit from the MEP constraint. In all these cases, the ptychography algorithm is tasked with solving for more than just a single sample and illumination. The additional information introduced by the MEP constraint will

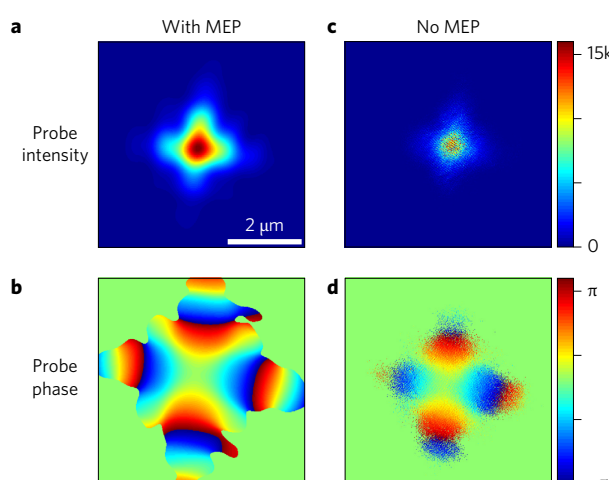


Figure 5 | Minimization of artefacts in the reconstructed illumination with probe enforcement. **a,b**, Intensity (**a**) and phase (**b**) of the EUV illumination at the sample plane with the MEP constraint. The intensity of the illumination is shown in detector counts. **c,d**, Intensity (**c**) and phase (**d**) of the illumination without the MEP constraint. Without the MEP constraint there is crosstalk between the illumination and sample leading to poor decoupling. The scale bar in **a** is common to all panels.

reduce the number of unknowns in the algorithm, helping with convergence and stability.

Future studies can employ the EUV and X-ray spectral region for chemical and elemental specificity. Furthermore, illumination with shorter wavelengths is possible using either tabletop high-harmonic sources or large-scale synchrotrons and X-ray free-electron lasers, which in the future can enable nanometre or even atomic-scale resolution of a broad range of next-generation nanoelectronics, data storage and nano-engineered systems.

Methods

Methods and any associated references are available in the [online version of the paper](#).

Received 24 October 2016; accepted 12 February 2017;
published online 20 March 2017

References

- Shapiro, D. A. *et al.* Chemical composition mapping with nanometre resolution by soft X-ray microscopy. *Nat. Photon.* **8**, 765–769 (2014).
- Donnelly, C. *et al.* Element-specific X-ray phase tomography of 3D structures at the nanoscale. *Phys. Rev. Lett.* **114**, 115501 (2015).
- Beckers, M. *et al.* Chemical contrast in soft X-ray ptychography. *Phys. Rev. Lett.* **107**, 208101 (2011).
- Rundquist, A. *et al.* Phase-matched generation of coherent soft X-rays. *Science* **280**, 1412–1415 (1998).
- Bartels, R. A. *et al.* Generation of spatially coherent light at extreme ultraviolet wavelengths. *Science* **297**, 376–378 (2002).
- Zhang, X. *et al.* Highly coherent light at 13 nm generated by use of quasi-phase-matched high-harmonic generation. *Opt. Lett.* **29**, 1357–1359 (2004).
- Ishikawa, T. *et al.* A compact X-ray free-electron laser emitting in the sub-Ångström region. *Nat. Photon.* **6**, 540–544 (2012).
- Miao, J., Ishikawa, T., Robinson, I. K. & Murnane, M. M. Beyond crystallography: diffractive imaging using coherent X-ray light sources. *Science* **348**, 530–535 (2015).
- Clark, J. N. *et al.* Ultrafast three-dimensional imaging of lattice dynamics in individual gold nanocrystals. *Science* **341**, 56–59 (2013).
- Leshem, B. *et al.* Direct single-shot phase retrieval from the diffraction pattern of separated objects. *Nat. Commun.* **7**, 10820 (2016).
- Odstrcil, M. *et al.* Ptxographic imaging with a compact gas-discharge plasma extreme ultraviolet light source. *Opt. Lett.* **40**, 5574–5577 (2015).
- Pfeifer, M. A., Williams, G. J., Vartanyants, I. A., Harder, R. & Robinson, I. K. Three-dimensional mapping of a deformation field inside a nanocrystal. *Nature* **442**, 63–66 (2006).
- Dierolf, M. *et al.* Ptxographic X-ray computed tomography at the nanoscale. *Nature* **467**, 436–439 (2010).
- Roy, S. *et al.* Lensless X-ray imaging in reflection geometry. *Nat. Photon.* **5**, 243–245 (2011).
- Sun, T., Jiang, Z., Strzalka, J., Ocola, L. & Wang, J. Three-dimensional coherent X-ray surface scattering imaging near total external reflection. *Nat. Photon.* **6**, 586–590 (2012).
- Sayre, D. Prospects for long wavelength X-ray microscopy and diffraction. *Imaging Processes Coherence Phys.* **112**, 229–235 (1980).
- Miao, J., Charalambous, P., Kirz, J. & Sayre, D. Extending the methodology of X-ray crystallography to allow imaging of micrometre-sized non-crystalline specimens. *Nature* **400**, 342–344 (1999).
- Chao, W., Harteneck, B., Liddle, J., Anderson, E. & Attwood, D. Soft X-ray microscopy at a spatial resolution better than 15 nm. *Nature* **435**, 1210–1213 (2005).
- Huang, X. *et al.* Signal-to-noise and radiation exposure considerations in conventional and diffraction X-ray microscopy. *Opt. Express* **17**, 13541–13553 (2009).
- Fienup, J. Reconstruction of an object from the modulus of its Fourier transform. *Opt. Lett.* **3**, 27–29 (1978).
- Fienup, J. R. Phase retrieval algorithms: a comparison. *Appl. Opt.* **21**, 2758–2769 (1982).
- Elser, V. Random projections and the optimization of an algorithm for phase retrieval. *J. Phys. A* **36**, 2995–3007 (2003).
- Marchesini, S. *et al.* X-ray image reconstruction from a diffraction pattern alone. *Phys. Rev. B* **68**, 140101 (2003).
- Luke, D. R. Relaxed averaged alternating reflections for diffraction imaging. *Inverse Probl.* **21**, 37–50 (2005).
- Thibault, P. & Guizar-Sicairos, M. Maximum-likelihood refinement for coherent diffractive imaging. *New J. Phys.* **14**, 063004 (2012).
- Shechtman, Y. *et al.* Phase retrieval with application to optical imaging: a contemporary overview. *IEEE Signal Process. Mag.* **32**, 87–109 (2015).
- Miao, J., Sayre, D. & Chapman, H. N. Phase retrieval from the magnitude of the Fourier transforms of nonperiodic objects. *J. Opt. Soc. Am. A* **15**, 1662–1669 (1998).
- Zürch, M. *et al.* Real-time and sub-wavelength ultrafast coherent diffraction imaging in the extreme ultraviolet. *Sci. Rep.* **4**, 7356 (2014).
- Rodenburg, J. M. *et al.* Hard-X-ray lensless imaging of extended objects. *Phys. Rev. Lett.* **98**, 034801 (2007).
- Rodenburg, J. M. Ptychography and related diffractive imaging methods. *Adv. Imag. Electron Phys.* **150**, 87–184 (2008).
- Thibault, P. *et al.* High-resolution scanning X-ray diffraction microscopy. *Science* **321**, 379–382 (2008).
- Guizar-Sicairos, M. & Fienup, J. Phase retrieval with transverse translation diversity: a nonlinear optimization approach. *Opt. Express* **16**, 7264–7278 (2008).
- Kane, D. J. Method and apparatus for determining wave characteristics from wave phenomena. US patent 6,219,142 B1 (2001).
- Maiden, A. & Rodenburg, J. An improved ptxographical phase retrieval algorithm for diffractive imaging. *Ultramicroscopy* **109**, 1256–1262 (2009).
- Seaberg, M. *et al.* Tabletop nanometer extreme ultraviolet imaging in an extended reflection mode using coherent Fresnel ptxography. *Optica* **1**, 39–44 (2014).
- Zhang, B. *et al.* High contrast 3D imaging of surfaces near the wavelength limit using tabletop EUV ptxography. *Ultramicroscopy* **158**, 98–104 (2015).
- Sayre, D. Some implications of a theorem due to Shannon. *Acta Crystallogr.* **5**, 843 (1952).
- Harada, T., Nakasui, M., Nagata, Y., Watanabe, T. & Kinoshita, H. Phase imaging of extreme-ultraviolet mask using coherent extreme-ultraviolet scatterometry microscope. *Jpn. J. Appl. Phys.* **52**, 06GB02 (2013).
- Shanblatt, E. R. *et al.* Quantitative chemically-specific coherent diffractive imaging of buried interfaces using a tabletop EUV nanoscope. *Nano Lett.* **19**, 5444–5450 (2016).
- Kapteyn, H. C., Murnane, M. M. & Christov, I. P. Extreme nonlinear optics: coherent X rays from lasers. *Phys. Today* **58**, 39–44 (2005).
- Thibault, P., Dierolf, M., Bunk, O., Menzel, A. & Pfeiffer, F. Probe retrieval in ptxographic coherent diffractive imaging. *Ultramicroscopy* **109**, 338–343 (2009).
- Putkunz, C. T. *et al.* Phase-diverse coherent diffractive imaging: high sensitivity with low dose. *Phys. Rev. Lett.* **106**, 013903 (2011).
- Henke, B. L., Gullikson, E. M. & Davis, J. C. X-ray interactions: photoabsorption, scattering, transmission, and reflection at $E = 50\text{--}30,000 \text{ eV}$, $Z = 1\text{--}92$. *Atom Data Nucl. Data Tables* **54**, 181–342 (1993).
- Thibault, P. & Menzel, A. Reconstructing state mixtures from diffraction measurements. *Nature* **494**, 68–71 (2013).
- Batey, D. J., Claus, D. & Rodenburg, J. M. Information multiplexing in ptxography. *Ultramicroscopy* **138**, 13–21 (2013).
- Edo, T. B. *et al.* Sampling in X-ray ptxography. *Phys. Rev. A* **87**, 053850 (2013).
- Batey, D. J. *et al.* Reciprocal-space up-sampling from real-space oversampling in X-ray ptxography. *Phys. Rev. A* **89**, 043812 (2014).
- Maiden, A. M., Humphry, M. J. & Rodenburg, J. M. Ptxographic transmission microscopy in three dimensions using a multi-slice approach. *J. Opt. Soc. Am. A* **29**, 1606–1614 (2012).
- Goddet, T. M., Suman, R., Humphry, M. J., Rodenburg, J. M. & Maiden, A. M. Ptxographic microscope for three-dimensional imaging. *Opt. Express* **22**, 12513–12523 (2014).

Acknowledgements

M.M.M. and H.C.K. acknowledge support from the Defense Advanced Research Projects Agency PULSE programme (DARPA-BAA-12-63-FP-004), the Gordon and Betty Moore Foundation Experimental Investigator programme in Emergent Phenomena in Quantum Systems (grant no. GBMF4538) and the National Science Foundation Science and Technology Centers (NSF STROBE, grant no. NSF DMR-1548924). D.F.G., C.L.P., C.B. and R.K. acknowledge Graduate Fellowship support from the Ford Foundation, the National Science Foundation and the National Defense Science and Engineering Graduate Fellowship Program. X.Z., D.E.A., M.M.M. and H.C.K. acknowledge the Department of Energy STTR/SBIR phase IIIB Grant (grant no. DE-SC0006514).

Author contributions

H.C.K. and M.M.M. conceived of the experiment. All authors designed aspects of the experiment, performed the research and wrote the paper. D.F.G. and G.F.M. characterized the source and collected the data sets. D.F.G. performed the reconstructions and data analysis. G.F.M. carried out the SEM imaging of the zone plate. D.E.A., D.F.G. and M.T. performed the probe enforcement simulations. X.Z., H.C.K., M.M.M. and B.R.G. designed the HHG source.

Additional information

Supplementary information is available in the [online version of the paper](#). Reprints and permissions information is available online at [www.nature.com/reprints](#). Publisher's note: Springer Nature remains neutral with regard to jurisdictional claims in published maps and institutional affiliations. Correspondence and requests for materials should be addressed to D.F.G.

Competing financial interests

E.R.S., C.L.P., M.T., D.F.G., D.E.A., G.F.M., M.M.M. and H.C.K. have submitted a patent disclosure based on this work. M.M.M. and H.C.K. are partial owners of Kapteyn-Murnane Laboratories Inc. who manufactured the ultrafast laser and EUV source.

Methods

Experimental layout. The driving laser was a KMLabs Dragon centred at a wavelength of 785 nm, with 2 mJ pulse energy, 23 fs pulse duration, and a repetition rate of 3 kHz. The laser was focused and coupled into a 150- μm -diameter capillary, filled with 500 torr of helium, and carefully engineered to phase-match the generation of harmonics at 13.5 nm. The second multilayer mirror had a radius of curvature of 100 mm. The angle of incidence on the mirrors was estimated to be $2 \pm 0.5^\circ$ from normal. The beam size at the focus was measured using a knife-edge method to be $\sim 2 \pm 0.5 \mu\text{m}$ in diameter. The EUV light was detected on an Andor iKon with an array of $2,048 \times 2,048$ square pixels (side length of $13.5 \mu\text{m}$). The collected diffraction patterns were binned by 2, on-chip, and cropped to 900×900 pixels. At each scan position, two accumulations were taken with 4.25 s exposures at 1 MHz pixel readout rate.

Image reconstructions. The reconstructions were carried out in four stages with the ePIE algorithm, as described in ref. 34. In one set of reconstructions, we modified the ePIE algorithm and implemented our MEP constraint. A binary mask was used to block the stray background light in the first two stages. In the first stage, we used a calculated probe through the beamline and an object guess of unity. The algorithm performed 950 iterations, with probe updates allowed after 100 iterations. In the second stage, we re-initialized the object guess to unity and fed in the probe from the end of stage 1. Stage 2 was allowed to run for 700 iterations with updates allowed to the probe after iteration 100. In the third stage, we used the probe from the end of stage 2 and the object guess was re-initialized to unity. At this stage, we let the algorithm fill in data in the masked-off background region. In other words, the modulus constraint was not enforced in the stray background region. Stage 3 ran for 10,000 iterations with probe updates allowed between iterations 2,000 and 9,000. Finally, in stage 4, we fed in both the object

and probe from the end of stage 3. The algorithm was allowed to continue to extrapolate values, and position correction was performed as described in ref. 50 between iterations 2,000 and 9,000 (ref. 50). The probe was allowed to update between iterations 2,000 and 9,000. The final reconstructions and retrieved probes, obtained after 10,000 iterations, are shown in Figs 3 and 5 and in the Supplementary Information. For NA values higher than the 0.54 presented in this work, the curvature of the diffraction on the Ewald sphere must be taken into account before carrying out the image reconstruction.

2+1D phase reconstruction. The intensity images of the ZP were used to create two binary masks: a mask for the PMMA features and a mask for the Si_3N_4 substrate. A threshold of 1/3 of the theoretical transmission of Si_3N_4 (ref. 43) was used to separate the materials. The phase of the substrate was fitted to a second-order plane. The fitted phase plane was subtracted from the entire phase image. Values less than $-\pi$ were wrapped around to lie between $-\pi$ and π . Within the PMMA mask, values less than three times the standard deviation of the substrate phase were increased by π to unwrap the phase. The phase values were converted to height using the reported index of refraction values in ref. 43 and a wavelength of 13.5 nm. The rendered image was interpolated onto a $4 \times$ larger grid and the vertical scale was scaled by 1/5.

Data availability. The data that support the plots within this paper and other findings of this study are available from the corresponding author upon reasonable request.

References

50. Zhang, F. *et al.* Translation position determination in ptychographic coherent diffraction imaging. *Opt. Express* **21**, 13592–13606 (2013).